



Universiteit
Leiden
The Netherlands

Changing-look event in NGC 3516: continuum or obscuration variability?

Mehdipour, M.; Kriss, G.A.; Brenneman, L.W.; Costantini, E.; Kaastra, J.S.; Branduardi-Raymont, G.; ... ; Mao, J.

Citation

Mehdipour, M., Kriss, G. A., Brenneman, L. W., Costantini, E., Kaastra, J. S., Branduardi-Raymont, G., ... Mao, J. (2022). Changing-look event in NGC 3516: continuum or obscuration variability? *The Astrophysical Journal*, 925(1). doi:10.3847/1538-4357/ac42ca

Version: Publisher's Version

License: [Creative Commons CC BY 4.0 license](https://creativecommons.org/licenses/by/4.0/)

Downloaded from: <https://hdl.handle.net/1887/3515508>

Note: To cite this publication please use the final published version (if applicable).



Changing-look Event in NGC 3516: Continuum or Obscuration Variability?

Missagh Mehdipour¹, Gerard A. Kriss¹, Laura W. Brenneman², Elisa Costantini^{3,4}, Jelle S. Kaastra^{3,5},

Graziella Branduardi-Raymont⁶, Laura Di Gesu⁷, Jacobo Ebrero⁸, and Junjie Mao^{3,9,10}

¹Space Telescope Science Institute, 3700 San Martin Drive, Baltimore, MD 21218, USA; mmehdipour@stsci.edu

²Center for Astrophysics | Harvard & Smithsonian, 60 Garden Street, Cambridge, MA 02138, USA

³SRON Netherlands Institute for Space Research, Niels Bohrweg 4, 2333 CA Leiden, The Netherlands

⁴Anton Pannekoek Institute, University of Amsterdam, Postbus 94249, 1090 GE Amsterdam, The Netherlands

⁵Leiden Observatory, Leiden University, PO Box 9513, 2300 RA Leiden, The Netherlands

⁶Mullard Space Science Laboratory, University College London, Holmbury St. Mary, Dorking, Surrey, RH5 6NT, UK

⁷Italian Space Agency (ASI), Via del Politecnico snc, I-00133, Roma, Italy

⁸Telespazio UK for the European Space Agency (ESA), European Space Astronomy Centre (ESAC), Camino Bajo del Castillo,s/n, E-28692 Villanueva de la Cañada, Madrid, Spain

⁹Department of Physics, Hiroshima University, 1-3-1 Kagamiyama, Higashihiroshima, Hiroshima 739-8526, Japan

¹⁰Department of Physics, University of Strathclyde, Glasgow G4 0NG, UK

Received 2021 August 9; revised 2021 December 6; accepted 2021 December 12; published 2022 January 27

Abstract

The Seyfert-1 galaxy NGC 3516 has undergone major spectral changes in recent years. In 2017 we obtained Chandra, NuSTAR, and Swift observations during its new low-flux state. Using these observations, we model the spectral energy distribution (SED) and the intrinsic X-ray absorption, and compare the results with those from historical observations taken in 2006. We thereby investigate the effects of the changing-look phenomenon on the accretion-powered radiation and the ionized outflows. Compared to its normal high-flux state in 2006, the intrinsic bolometric luminosity of NGC 3516 was lower by a factor of 4–8 during 2017. Our SED modeling shows a significant decline in the luminosity of all the continuum components from the accretion disk and the X-ray source. As a consequence, the reprocessed X-ray emission lines have also become fainter. The Swift monitoring of NGC 3516 shows remarkable X-ray spectral variability on short (weeks) and long (years) timescales. We investigate whether this variability is driven by obscuration or the intrinsic continuum. We find that the new low-flux spectrum of NGC 3516, and its variability, do not require any new or variable obscuration, and instead can be explained by changes in the ionizing SED that result in the lowering of the ionization of the warm-absorber outflows. This in turn induces enhanced X-ray absorption by the warm-absorber outflows, mimicking the presence of new obscuring gas. Using the response of the ionized regions to the SED changes, we place constraints on their densities and locations.

Unified Astronomy Thesaurus concepts: Active galactic nuclei (16); X-ray active galactic nuclei (2035); High energy astrophysics (739); Seyfert galaxies (1447); Spectroscopy (1558); X-ray observatories (1819)

1. Introduction

Outflows from active galactic nuclei (AGN) may couple the supermassive black holes (SMBHs) to their host galaxies. The observed relations between SMBHs and their host galaxies, such as the M - σ relation (Ferrarese & Merritt 2000), indicate that SMBHs and their host galaxies are likely co-evolved through a feedback mechanism. Ionized-AGN winds, also referred to as warm-absorber outflows, may play an important role in connecting AGN to their environment (see, e.g., Laha et al. 2021). High-resolution spectroscopy in the UV and X-ray energy bands, in particular with the Hubble Space Telescope (HST), Chandra, and XMM-Newton, has been instrumental for studying the ionized outflows in AGN. However, many aspects and physical properties of the AGN outflows are still poorly understood. Spectral variability is a hallmark of AGN, yet deciphering its nature and origin remains challenging. As variability can arise from either the accretion-powered radiation or nuclear obscuration/absorption in our line of sight, distinction between these two interpretations is important for advancing our knowledge of the role and impact of outflows in AGN.

NGC 3516 is a notable Seyfert-1 galaxy. Due to its high brightness in both UV and X-rays, and its prominent and clear AGN absorption features, it has been an ideal laboratory for studying the AGN warm-absorber outflows with high-resolution spectroscopy. Over the past few decades, there have been many UV and X-ray case studies of the ionized outflows in NGC 3516, such as publications by Voit et al. (1987), Kriss et al. (1996a, 1996b), Mathur et al. (1997), Costantini et al. (2000), Kraemer et al. (2002), Netzer et al. (2002), Markowitz et al. (2008), Turner et al. (2008), Turner et al. (2011), Mehdipour et al. (2010), Holczer & Behar (2012), Huerta et al. (2014), and Dunn et al. (2018). Historically, NGC 3516 has been a remarkably variable AGN, showing changes in both the intrinsic continuum (e.g., Mehdipour et al. 2010; Noda et al. 2016; Ilić et al. 2020) and the intrinsic absorption by the ionized outflows (e.g., Costantini et al. 2000; Turner et al. 2008; Dunn et al. 2018). However, over the last few years, NGC 3516 underwent a major spectral change, classifying it as a “changing-look AGN” (see, e.g., Shapovalova et al. 2019).

Changing-look AGN are considered those that alter their appearance from type-1 to type-2 AGN (or vice versa), where the common classification of type-1 and type-2 AGN is based on the optical emission lines, with broad lines predominantly seen in the type-1 AGN. Some notable examples of changing-look AGN are Mrk 590 (Denney et al. 2014), Mrk 1018



Original content from this work may be used under the terms of the [Creative Commons Attribution 4.0 licence](https://creativecommons.org/licenses/by/4.0/). Any further distribution of this work must maintain attribution to the author(s) and the title of the work, journal citation and DOI.

(Cohen et al. 1986), NGC 1566 (Oknyansky et al. 2019), SDSS J015957.64 + 003310.5 (LaMassa et al. 2015), NGC 2617 (Shappee et al. 2014), and 1ES 1927 + 654 (Trakhtenbrot et al. 2019). Systematic searches using large surveys have revealed an increasing number of other changing-look AGN; see MacLeod et al. (2016), Ruan et al. (2016), and Yang et al. (2018). Importantly, major spectral transformations of changing-look AGN are seen in both the intrinsic continuum and the emission lines of the AGN (see, e.g., LaMassa et al. 2015). While in general the nature of the changing-look phenomenon may ultimately be attributed to the AGN-accretion activity, the physical mechanisms responsible for the transformation are not fully understood. Over the years, different scenarios have been postulated for changing-look AGN, such as large changes in the mass accretion rate (e.g., Elitzur et al. 2014; Runnoe et al. 2016; Noda & Done 2018), transient-nuclear obscuration of the central ionizing source (e.g., Tran et al. 1992; Matt et al. 2003; Dehghanian et al. 2019), or in some cases tidal disruption events (e.g., Komossa 2015; Merloni et al. 2015).

In the case of NGC 3516, Shapovalova et al. (2019) first reported about its changing look from a high-flux state to a low-flux state. Since then there have been further studies of the changing-look behavior of the optical emission lines from the broad-line region (BLR), and its reverberation mapping, by Feng et al. (2021) and Oknyansky et al. (2021). In this paper, by deriving the broadband spectral energy distribution (SED), and photoionization modeling, we aim to determine the intrinsic optical-UV-X-ray continuum and the X-ray absorption in NGC 3516, before and during the changing-look event. This enables us to examine the two competing scenarios of a change in the accretion-powered radiation versus the appearance of transient-obscuring gas. To this end, we obtained two sets of Chandra Low Energy Transmission Grating (LETG) and NuSTAR observations in 2017 December during the depth of the low-flux state in NGC 3516. We also obtained Neil Gehrels Swift Observatory monitoring observations in 2017, taken contemporaneously with Chandra and NuSTAR, using all of the six primary optical and UV filters of the Swift/UVOT. This facilitates deriving the optical/UV part of the continuum in our SED modeling. The two sets of Chandra and NuSTAR observations were separated by about three weeks to probe the observed X-ray spectral variability that was evident in the Swift monitoring of NGC 3516 (see Figure 1). These new 2017 data taken during the low-flux state, and the archival XMM-Newton and Swift data taken in 2006 during the high-flux state, are used for our modeling in this paper to establish the change in the SED and the change in the X-ray absorption in NGC 3516.

Figure 1 shows the Swift lightcurve of NGC 3516 from 2012 January to 2021 July, revealing the long-term behavior of the changing-look phenomenon. The UV, and soft and hard X-ray fluxes, already appear to decline in 2012 when Swift started to extensively monitor the AGN. For comparison the UV and X-ray flux levels from 2006 are also over-plotted in Figure 1 (horizontal dashed lines), when NGC 3516 was in its high-flux state according to archival Swift and XMM-Newton observations (see, e.g., Turner et al. 2008; Mehdipour et al. 2010). The vertical dotted lines in the Swift lightcurve of Figure 1 correspond to when our joint Chandra/LETG and NuSTAR observations were taken in 2017 December at the low-flux state. The bottom panel of Figure 1 shows the X-ray hardness ratio (R), defined as $R = (H - S)/(H + S)$, where H and S are

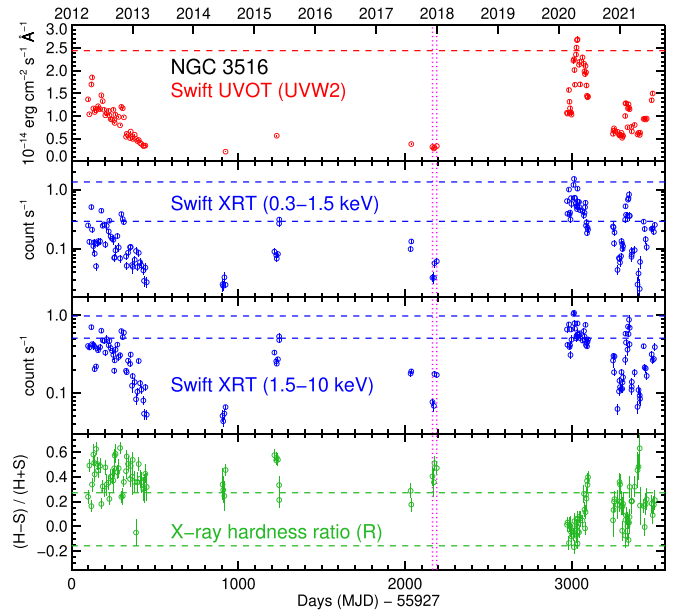


Figure 1. Swift lightcurve of NGC 3516 spanning from 2012 January to 2021 July. The bottom panel shows the X-ray hardness ratio (R), defined as $R = (H - S)/(H + S)$, where H and S are the Swift/XRT count rate fluxes in the hard (1.5–10 keV) and soft (0.3–1.5 keV) bands, respectively. The vertical dotted lines in magenta indicate the time of our joint Chandra/LETG and NuSTAR observations (Obs. 1 and Obs. 2) taken in 2017 December when NGC 3516 was in its low-flux state. The horizontal dashed lines in each panel indicate the range of flux or hardness ratio seen in 2006 during the high-flux state, obtained from the archival XMM-Newton and Swift observations. We use our spectral model fitted to the 2006 XMM-Newton observation (Figure 3) to calculate the equivalent Swift/XRT count rates for the purpose of displaying the horizontal lines on this figure. A single Swift/UVOT (UVW2) observation was taken in 2006, and thus only one horizontal line is plotted in the top panel. The tick marks on the top axis indicate the start of each year for reference. The displayed data include the effects of absorption and reddening. Major declines in the UV and X-ray fluxes since 2012 (top and middle panels), as well as significant X-ray spectral hardening and variability (bottom panels), are evident in the Swift lightcurve. In 2020 there is a recovery in the flux and the hardness ratio, reaching the 2006 levels, followed by another decline toward the end of the year and further variability in 2021.

the Swift/XRT count rate fluxes in the hard (1.5–10 keV) and soft (0.3–1.5 keV) bands, respectively. As well as significant spectral hardening in the low-flux state (Figure 1, bottom panel), the hardness ratio R shows remarkable X-ray spectral variability on weeks timescales. The Swift monitoring of NGC 3516 (Figure 1) shows that the UV and X-ray fluxes recovered in 2020, and the hardness ratio reached the soft levels seen during the high-flux state of 2006. Oknyansky et al. (2021) have also reported about the reemergence of NGC 3516 to its high-flux state in 2020. Furthermore, Figure 1 shows that toward the end of 2020 there is another decline in flux, as well as significant variability throughout 2021.

The structure of the paper is as follows. In Section 2, we describe our observations and the data reduction and processing. The modeling of the spectra and the results are presented in Section 3. We discuss and interpret our findings in Section 4, and give concluding remarks in Section 5. Our spectral analysis and modeling were done using the SPEX package (Kaastra et al. 1996, 2020) v3.06.01. We use C-statistics (Cash 1979) for fitting the data as it provides the most robust method for X-ray spectral fitting with low count rate statistics; for more information about C-statistics and its implementation in SPEX, we refer to Kaastra (2017) and the SPEX manual (Kaastra et al. 2020). The model parameter errors are given at the 1σ

Table 1
Log of Our NGC 3516 Observations Taken in 2017

Observatory	Observation ID	Observation Date yyyy-mm-dd	Length (ks)
Chandra/LETG	20877 (Obs. 1)	2017-12-05	24.9
Chandra/LETG	19519 (Obs. 1)	2017-12-07	35.8
Chandra/LETG	20878 (Obs. 1)	2017-12-11	21.0
Chandra/LETG	20904 (Obs. 2)	2017-12-26	35.8
Chandra/LETG	19520 (Obs. 2)	2017-12-29	19.5
Chandra/LETG	20905 (Obs. 2)	2017-12-30	27.5
NuSTAR	60302016002 (Obs. 1)	2017-12-05	28.8
NuSTAR	60302016004 (Obs. 1)	2017-12-07	32.7
NuSTAR	60302016006 (Obs. 1)	2017-12-11	33.0
NuSTAR	60302016008 (Obs. 2)	2017-12-26	22.3
NuSTAR	60302016010 (Obs. 2)	2017-12-28	34.1
NuSTAR	60302016012 (Obs. 2)	2017-12-30	33.3
Swift	00035462010	2017-12-04	1.5
Swift	00035462012	2017-12-13	0.8
Swift	00035462013	2017-12-16	1.1
Swift	00035462014	2017-12-30	1.2

Note. The “Obs. 1” and “Obs. 2” refer to two sets of spectra, separated by about three weeks, which we model in this paper. In addition to our 2017 Swift observations shown above, we make use of other Swift data, spanning from 2006 to 2021, to help characterize the long-term X-ray and optical/UV variability of NGC 3516. We also fit an archival 2006 XMM-Newton/EPIC-pn spectrum (Obs. ID: 0401210501, 68 ks), taken from Mehdipour et al. (2010), where we studied the warm-absorber of NGC 3516.

confidence level. We adopt a luminosity distance of 38.1 Mpc (redshift $z = 0.008836$; Keel 1996) in our calculations with the cosmological parameters $H_0 = 70 \text{ km s}^{-1} \text{ Mpc}^{-1}$, $\Omega_\Lambda = 0.70$, and $\Omega_m = 0.30$.

2. Observations and Data Reduction

The observation logs of our NGC 3516 data are provided in Table 1. We model two sets of joint Chandra/LETG and NuSTAR observations, which we refer to as “Obs. 1” and “Obs. 2.” The two observations were taken in 2017 December, separated by about three weeks. We also include the associated contemporaneous Swift/UVOT data in our modeling of each observation. In Figure 2, the new Swift/UVOT, Chandra/LETG, and NuSTAR spectra (Obs. 1 and 2) taken during the changing-look low-flux state in 2017 December are compared with the Swift/UVOT and XMM-Newton/EPIC-pn spectra taken at the high-flux state in 2006. The transformation in shape and flux of the optical-UV-X-ray spectrum between the two epochs is striking. By modeling the new 2017 spectra, and comparing the results with those from the archival 2006 observations, we investigate the effects of the changing-look event on the intrinsic continuum and the ionized outflows in NGC 3516.

For scheduling reasons, each Chandra and NuSTAR observation was split into three separate exposures spanning a few days (Table 1). For our spectral modeling, we stack the individual exposures of each observation to improve the signal-to-noise ratio. The variability between the individual exposures is not too much to prevent stacking of the spectra. All the X-ray spectra were optimally binned according to Kaastra & Bleeker (2016) for fitting in SPEX. For each 2017 observation, we

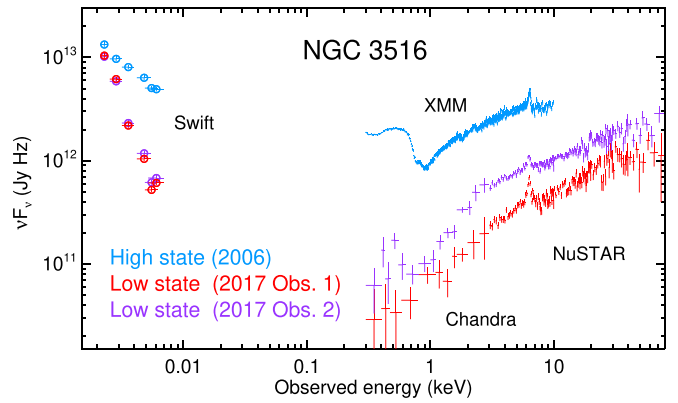


Figure 2. Optical/UV and X-ray spectra of NGC 3516 taken during the high-flux state in 2006 and the low-flux state in 2017. The data are from Chandra/LETG (2017), NuSTAR (2017), XMM-Newton/EPIC-pn (2006), and Swift/UVOT (2006 and 2017). The displayed data include the host galaxy emission and the effects of intrinsic and Galactic absorption and reddening. The displayed X-ray spectra have been binned for clarity of presentation. The best-fit model to these data is shown in Figure 3 and the derived intrinsic continuum model in Figure 4. Transformation in shape and flux of the multi-wavelength spectrum between the two epochs is evident.

jointly fitted the spectra from Chandra/LETG (0.3–3 keV), NuSTAR (3–78 keV), and the Swift/UVOT optical/UV filters.

In Mehdipour et al. (2010), we studied the warm-absorber in NGC 3516 using XMM-Newton RGS and EPIC-pn spectra taken in 2006 during the normal high-flux state. To compare the SED models of the low-flux and high-flux states, we also fit one of the 2006 XMM-Newton/EPIC-pn spectra (Obs. ID: 0401210501, 68 ks) over 0.3–10 keV. The data reduction of this EPIC-pn spectrum is described in Mehdipour et al. (2010). As the Optical Monitor data of the 2006 XMM-Newton observations were all taken in just one filter (*U*), for the purpose of deriving the optical/UV part of the SED, we make use of the Swift/UVOT exposures that were taken in six optical and UV filters in 2006 (*V*, *B*, *U*, *UVW1*, *UVM2*, and *UVW2*), and fit them together with the 2006 EPIC-pn spectrum. The reduction and processing of the Chandra/LETG, NuSTAR, and Swift data are described as follows in Sections 2.1, 2.2, and 2.3, respectively.

2.1. Chandra/LETG Data

Our Chandra observations of NGC 3516 were taken with the LETG (Brinkman et al. 2000) grating and the HRC-S camera. The data were reduced using the Chandra Interactive Analysis of Observations (CIAO; Fruscione et al. 2006) v4.9 software and the HEASARC Calibration Database (CALDB) v4.7.3. The `chandra_repro` script of CIAO and its associated tools were used for the reduction of the data and production of the final grating products (PHA2 spectra, RMF and ARF response matrices). The \pm first-order spectra and their response matrices were combined using the CIAO `combine_grating_spectra` script.

2.2. NuSTAR Data

The NuSTAR (Harrison et al. 2013) observations were reduced using the NuSTAR Data Analysis Software (NUS-TARDAS v.1.8.0) and CALDB calibration files of HEASoft v6.22. The data were processed with the standard pipeline script `nupipeline` to produce level 1 calibrated and level 2 cleaned event files. The data from the South Atlantic Anomaly

passages were filtered out, and the event files were cleaned with the standard depth correction. The source was extracted from a circular region (radius = $75''$), with the background extracted from a source-free area of equal size on the same detector. The `nuproducts` script was run to create level 3 products (spectra, ARF and RMF response files) for each of the two hard X-ray telescope modules (FPMA and FPMB) on board NuSTAR. For each NuSTAR observation, the spectra and corresponding response matrices of the two telescopes were combined using the `mathpha`, `addrmf`, and `addarf` tools of the HEASoft package.

2.3. Swift/XRT and UVOT Data

For the Swift (Gehrels et al. 2004) X-ray Telescope (XRT; Burrows et al. 2005) data reduction, we used the procedure detailed in Evans et al. (2007, 2009), which is an enhanced version of the standard Swift processing pipeline including some modifications. This tool is made available online on the UK Swift Science Data Centre. The XRT instrument was operated in the Photon Counting (PC) mode. The default grades of 0–12 in the PC mode were used for event selection. The data were corrected for bad pixels and effects of vignetting and PSF to produce cleaned event files. The optimum extraction radius for data products depends on the count rate as reported in Evans et al. (2007, 2009), which for NGC 3516 mostly corresponds to an extraction radius of $70''.8$. The XRT lightcurves at soft (0.3–1.5 keV) and hard (1.5–10 keV) X-ray energies were constructed from each Swift snapshot, as described in Evans et al. (2007).

The Swift/UVOT (Roming et al. 2005) data from the Image-mode operations were taken with the six primary photometric filters of *V*, *B*, *U*, *UVW1*, *UVM2*, and *UVW2*. The `uvotsource` tool was used to perform aperture photometry using a circular aperture diameter of $10''$. The standard instrumental corrections and calibrations according to Poole et al. (2008) were applied. For the purpose of spectral fitting with SPEX, the count rate and the corresponding response matrix file for each filter were created.

3. Spectral Modeling

Here we present our modeling of the spectral components that form the observed SED in NGC 3516. This consists of simultaneously modeling the continuum components (described in Section 3.1) and the X-ray absorption components (described in Section 3.2). We derive the SED and the intrinsic X-ray absorption for Obs. 1 and Obs. 2, using Chandra/LETG, NuSTAR, and Swift/UVOT data, taken in 2017 December during the low-flux state of NGC 3516. For comparison with the 2017 model, we also model the archival XMM-Newton/EPIC-pn and Swift/UVOT data taken in 2006 (described in Section 2) to obtain the SED in the normal high-flux state of NGC 3516.

3.1. Broadband Continuum Modeling

The broadband continuum model that we apply to fit the NGC 3516 data (Figure 3) consists of three continuum components in SPEX: (1) a `comt` component that models the optical/UV thermal continuum from the accretion disk and the associated *soft X-ray excess* by warm Comptonization, (2) a `pow` component that models the primary X-ray power law, and (3) a `refl` neutral-reflection component that produces the Fe K

α line and the Compton hump at hard X-rays. Such modeling of the broadband continuum has previously been carried out for other similar AGN, such as the archetypal Seyfert-1 galaxy NGC 5548 in Mehdipour et al. (2015).

Our previous XMM-Newton study of NGC 3516 (Mehdipour et al. 2010) shows a clear presence of a *soft X-ray excess* component in the normal high-flux state of NGC 3516 in 2006. Here we model the soft excess in NGC 3516 with warm Comptonization, which multi-wavelength studies of other similar Seyfert-1 AGN have found to be a viable explanation (see, e.g., Mehdipour et al. 2011; Done et al. 2012; Mehdipour et al. 2015; Kubota & Done 2018; Petrucci et al. 2018, 2020; Porquet et al. 2018). In this explanation of the soft excess, the seed disk photons are up-scattered in a warm, optically thick corona to produce the extreme UV (EUV) continuum and the soft X-ray excess as its tail at higher energies. We note that this is one plausible explanation proposed in the literature for the origin of the soft X-ray excess in AGN (relativistic ionized reflection is another explanation; Crummy et al. 2006), yet it is sufficient for our purpose of comparing the high-flux and low-flux states of NGC 3516 SEDs. The parameters of the `comt` model are its normalization, seed photon temperature T_{seed} , electron temperature T_e , and optical depth τ of the up-scattering corona. To limit the number of free parameters while still providing a good fit, some of the `comt` parameters of different observations are coupled together as shown in Table 2, where the best-fit parameters of the continuum components are given.

The X-ray power law (`pow`) represents the Compton up-scattering of the seed disk photons in an optically thin and hot corona. For each observation, we fit the normalization and the photon index Γ of the `pow` model. The intrinsic power-law continuum then undergoes reprocessing, modeled by the `refl` reflection model in SPEX, which computes the Fe K α line according to Zycki & Czerny (1994), and the Compton-reflected continuum according to Magdziarz & Zdziarski (1995), as described in Zycki et al. (1999). For the 2006 observation, the normalization and the photon index Γ of the illuminating power law for `refl` are coupled to those of the `pow` component. For the 2017 observations (i.e., Obs. 1 and 2), the normalization and Γ of `refl` are coupled to the average of the `pow` model for the two observations, representing a time-averaged illuminating power law that is reflected in the 2017 epoch.

The high-energy exponential cutoff (E_{cut}) of `pow` and the incident power law for `refl` were coupled together and fitted as one parameter for all the observations. We find the best-fit model to the NuSTAR spectra favors $E_{\text{cut}} > 1$ MeV, which minimizes the excess fit residuals at the higher-energy part of the NuSTAR spectra. We thus fixed E_{cut} to 1 MeV in our SED modeling. A low-energy exponential cutoff was also applied to the power-law continuum at the far-UV (13.6 eV) to prevent it from exceeding the energy of the seed photons from the disk. The ionization parameter of `refl` was set to zero to produce a neutral-reflection component, which is consistent with the observed neutral Fe K α line in NGC 3516 (Mehdipour et al. 2010). In our modeling, we fitted the reflection fraction parameter of the `refl` model for each observation.

In our modeling of the optical/UV data, we took into account the host galaxy starlight emission and the contribution of AGN emission lines in the Swift/UVOT filters. We used the galactic bulge template model of Kinney et al. (1996), and the NGC 3516 host galaxy flux measured by Bentz et al. (2013)

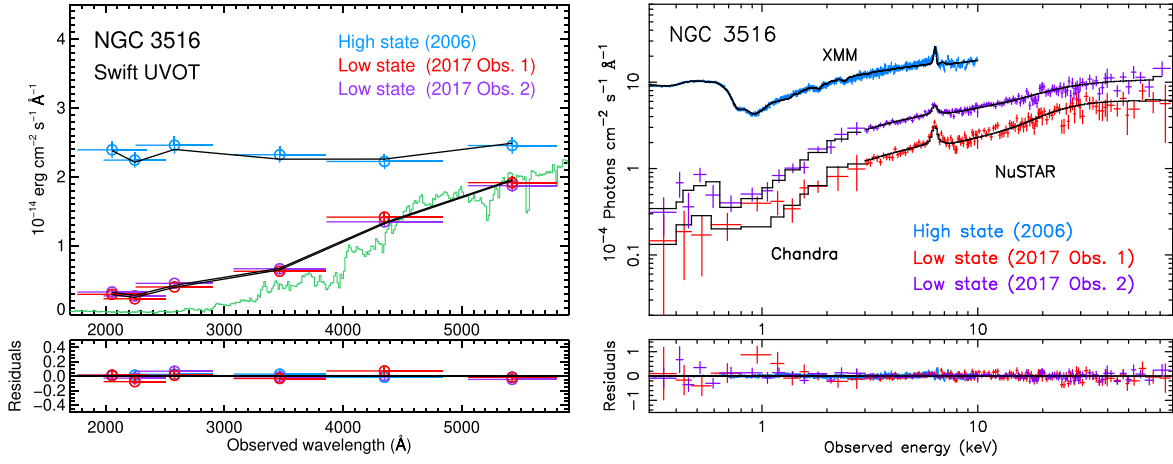


Figure 3. Best-fit *SPEX* model to the Swift/UVOT, Chandra/LETG, and NuSTAR spectra of Obs. 1 and Obs. 2 taken during the low-flux state in 2017 December, compared with the best-fit model to the Swift/UVOT and XMM-Newton/EPIC-pn data taken in the high-flux state in 2006. The optical/UV data are shown in the left panels and the X-ray data in the right panels. The best-fit model for each data set is shown as a black line. Residuals of the fit, defined as “(data–model)/model,” are displayed in the bottom panels. The model for the host galaxy stellar emission is shown in green in the top left panel. The displayed X-ray spectra have been binned for clarity of presentation. The intrinsic broadband continuum models corresponding to these best fits are shown in Figure 4.

Table 2

Best-fit Parameters of the Broadband Continuum Model Components for NGC 3516, Derived from Modeling the Normal High-flux State Observation Taken in 2006, and the Low-flux State Obs. 1 and 2 Taken in 2017

Parameter	Value
Disk component: optical-UV and the soft X-ray excess (<i>comt</i>):	
Normalization	2.9 ± 0.1 (2006) 0.3 ± 0.1 (Obs. 1) 0.4 ± 0.1 (Obs. 2)
T_{seed} (eV)	0.70 ± 0.02 (2006) 0.46 ± 0.08 (Obs. 1 and 2, coupled)
T_c (keV)	0.13 ± 0.01 (2006) 0.13 ± 0.01 (Obs. 1 and 2, coupled)
Optical depth τ	28 ± 3 (all observations, coupled)
Primary X-ray power-law component (<i>pow</i>):	
Normalization	27.3 ± 0.1 (2006) 2.6 ± 0.2 (Obs. 1) 5.7 ± 0.4 (Obs. 2)
Photon index Γ	1.87 ± 0.02 (2006) 1.75 ± 0.02 (Obs. 1) 1.73 ± 0.02 (Obs. 2)
X-ray reflection component (<i>refl</i>):	
Reflection fraction	0.53 ± 0.03 (2006) 0.61 ± 0.03 (Obs. 1) 0.61 ± 0.03 (Obs. 2)
C-stat / expected C-stat=1758 / 1100 (2006)	
C-stat / expected C-stat=2218 / 1896 (Obs. 1)	
C-stat / expected C-stat=2184 / 1908 (Obs. 2)	

Note. The normalization of the Comptonized disk component (*comt*) is in units of 10^{55} photons $\text{s}^{-1} \text{keV}^{-1}$. The power-law normalization of the *pow* and *refl* components is in units of 10^{50} photons $\text{s}^{-1} \text{keV}^{-1}$ at 1 keV. For the 2006 observation, the normalization and the photon index Γ of the incident power law for *refl* are coupled to those of the primary power-law *pow*. For Obs. 1 and 2, the normalization and Γ of *refl* were coupled to the average of the *pow* model for the two observations, representing a time-averaged illuminating power law for reflection in the 2017 epoch. The high-energy exponential cutoff of the power law for both *pow* and *refl* is fixed to 1 MeV as described in Section 3.1. The intrinsic luminosities of the continuum components for each observation are provided in Table 3.

from HST imaging, to calculate the corresponding stellar emission model for the $10''$ circular aperture of UVOT. This model is shown in Figure 3 (top left panel). To correct for the contribution of the AGN emission lines to the UVOT photometric filters (2% to 5%), we used the template model derived in Mehdipour et al. (2015) for the archetypal Seyfert-1 galaxy NGC 5548, and normalized this model to the $H\beta$ flux of NGC 3516. The $H\beta$ flux was taken from the long-term optical monitoring study of NGC 3516 by Shapovalova et al. (2019), which reports that, during the 2006 high-flux state, the $H\beta$ flux is about $9 \times 10^{-13} \text{ erg cm}^{-2} \text{ s}^{-1}$, and in the 2017 low-flux state, it is about $1 \times 10^{-13} \text{ erg cm}^{-2} \text{ s}^{-1}$. We correct for the foreground Milky Way extinction in our line of sight to NGC 3516, $E(B - V) = 0.037$ (Schlafly & Finkbeiner 2011), using the *ebv* model in *SPEX*, which uses the extinction curve of Cardelli et al. (1989), including the update for near-UV given by O’Donnell (1994). The ratio of total to selective extinction $R_V = A_V/E(B - V)$ was fixed to 3.1.

Figure 3 shows our best-fit model to the 2006 (Swift/UVOT and XMM-Newton/EPIC-pn) and the 2017 Obs. 1 and Obs. 2 (Swift/UVOT, Chandra/LETG, and NuSTAR) spectra. The modeling takes into account the X-ray absorption described below in Section 3.2. The best-fit parameters of the *comt*, *pow*, and *refl* components for each observation are given in Table 2. The corresponding intrinsic luminosities of the continuum components for each observation are shown in Table 3. Figure 4 displays the intrinsic continuum SED model derived from the 2006 and the 2017 Obs. 1 and 2 data, showing how the individual continuum components change between the observations. All continuum components of the NGC 3516 SED (*comt*, *pow*, and *refl*) have become fainter in the low-flux changing-look state seen in 2017.

3.2. X-Ray Absorption and Photoionization Modeling

In our X-ray absorption modeling, we first take into account the continuum and line absorption by the diffuse interstellar medium (ISM) in the Milky Way. This is done using the *hot* model in *SPEX* (de Plaa et al. 2004; Steenbrugge et al. 2005). This model calculates the transmission of a plasma in

Table 3

Intrinsic Luminosities of NGC 3516 for the Normal High-flux State in 2006, and the Changing-look Low-flux State in 2017 Obs. 1 and 2

Luminosity	2006 (10^{43} erg s $^{-1}$)	2017 Obs. 1 (10^{43} erg s $^{-1}$)	2017 Obs. 2 (10^{43} erg s $^{-1}$)
L_{comt}	5.5	0.5	0.6
L_{pow}	5.7	0.8	1.9
L_{refl}	0.8	0.2	0.2
L_{opt}	0.5	0.04	0.06
L_{UV}	1.7	0.1	0.2
L_{EUV}	2.9	0.2	0.3
L_{soft}	1.3	0.1	0.2
L_{hard}	1.0	0.1	0.3
L_{ion}	6.4	0.6	1.0
L_{bol}	12.0	1.5	2.7

Note. The intrinsic luminosities are derived from our broadband continuum modeling described in Section 3.1, using the Comptonized disk (L_{comt}), power law (L_{pow}), and the reflection (L_{refl}) components, shown in Figure 4 and Table 2. The luminosities L_{comt} , L_{pow} , and L_{refl} are calculated over the entire energy band (10^{-6} – 10^6 keV). The intrinsic luminosity in the optical band (L_{opt}) is calculated over 4000–7000 Å, UV (L_{UV}) over 1000–4000 Å, EUV (L_{EUV}) over 100–1000 Å, soft X-ray (L_{soft}) over 0.3–1.5 keV, and hard X-ray (L_{hard}) over 1.5–10 keV. The ionizing luminosity L_{ion} is calculated over 1–1000 Ryd, which is used in the definition of the ionization parameter ξ . The bolometric luminosity L_{bol} is the total intrinsic luminosity of the broadband continuum over 10^{-6} – 10^6 keV, calculated as the sum of the intrinsic luminosities of the continuum components L_{comt} , L_{pow} , and L_{refl} .

collisional ionization equilibrium at a given temperature, which for neutral ISM is set to the minimum temperature of the model at 0.008 eV. The total Galactic N_{H} column density was fixed to 4.04×10^{20} cm $^{-2}$ (Willingale et al. 2013), which is the sum of the atomic and molecular hydrogen components of the ISM in our line of sight to NGC 3516.

Our modeling of the ionized warm-absorber in NGC 3516 is carried out using the `pion` model (Mehdipour et al. 2016a; Miller et al. 2015) in `SPEX`. This self-consistent model calculates both the photoionization equilibrium solution and the spectrum, using the SED model that is simultaneously fitted to the data in `SPEX`. Previous spectroscopic studies of NGC 3516 (e.g., Turner et al. 2008; Mehdipour et al. 2010; Holzer & Behar 2012) have shown the clear presence of the intrinsic X-ray absorption by the warm-absorber in this AGN. In Mehdipour et al. (2010), we derived a model for the warm-absorber using XMM-Newton (RGS and EPIC-pn) observations taken in 2006. During this epoch, NGC 3516 was in its normal high-flux state, and thus the features of the warm-absorber were detected with high signal-to-noise ratio. The modeling of Mehdipour et al. (2010) shows that the warm-absorber consists of three ionization components.

Here we make use of the warm-absorber model derived by Mehdipour et al. (2010). However, in Mehdipour et al. (2010), an older version of the `SPEX` code was used (v2.01.02), and over the past decade, there have been significant advances and changes in the atomic data and plasma models of the `SPEX` code. Therefore, since here we are using the latest code, we re-fitted the 2006 spectrum. The column density N_{H} and ionization parameter ξ (defined by Krolik et al. 1981) of the three warm-absorber components of Mehdipour et al. (2010) were re-fitted to take into account changes between the codes. The other warm-absorber parameters (velocities and covering fractions) were kept to those measured by Mehdipour et al.

(2010). In our modeling in this paper, the abundances of the warm-absorber, and that of the Galactic absorption, are fixed to the proto-solar values of Lodders et al. (2009). In our model set-up, the ionizing SED first passes through the highest ionization component of the warm-absorber (Comp 1) and last through the lowest one (Comp 3). The N_{H} and ξ of the warm-absorber components for the 2006 observation are given in Table 4.

In our modeling of the low-flux state 2017 Obs. 1 and 2 spectra, we adopt the above warm-absorber model, which is from a normal average-level XMM-Newton observation taken in 2006 (Obs. ID: 0401210501). In the low-flux state of NGC 3516, the X-ray continuum is strongly diminished (Figures 2, 3, and 4). For this reason, the individual absorption lines are not detected with sufficient signal-to-noise ratio to enable the high-resolution X-ray spectral analysis. We therefore cannot independently model the warm-absorber to determine its properties, in particular the ionization parameter and the velocity. Thus, in our modeling of the 2017 data, we keep the persistent warm-absorber parameters fixed to those obtained from 2006, while the ionization parameters ξ of the components are self-consistently lowered in response to the intrinsic dimming of the SED. The total column density, covering fraction, and the velocity of the warm-absorbers in the best-studied AGN (such as NGC 5548) are found to remain persistent over long times, while responding to the ionizing radiation (see, e.g., Arav et al. 2015). Similarly, in the case of NGC 3516, the warm-absorbers seen in X-rays in 1995 (Kriss et al. 1996b) and 2006 (Mehdipour et al. 2010) are consistent with each other. Therefore, for the 2017 observations, the 2006 warm-absorber parameters are not re-fitted, but rather the ionization parameter of each component is automatically computed by `pion` according to the low-flux SED of each observation in 2017 (Figure 4). The lowered ionization parameters of the warm-absorber components for the 2017 observations are shown in Table 4. Importantly, the warm-absorber in 2017 is *de-ionized*, thus causing a higher opacity and producing a stronger absorption than in 2006, which can be seen in the X-ray transmission model shown in Figure 5. Finally, we tested freeing ξ of the warm-absorber components for the 2017 observations. This did not make a significant improvement to the best-fit model, and the ξ parameters remained consistent with the above “de-ionization” model.

Such de-ionization of the warm-absorber has been previously presented in NGC 5548 (Kaastra et al. 2014; Arav et al. 2015) and NGC 3783 (Mehdipour et al. 2017; Kriss et al. 2019a), in the context of shielding of the ionizing source by nuclear obscuring winds. However, here in the case of NGC 3516, the de-ionization is instead caused by the dimming of the intrinsic SED as a consequence of the changing-look phenomenon. Interestingly, we find that, as a result of the enhanced continuum absorption by the de-ionized warm-absorber, no additional absorption of the continuum is required to fit the 2017 X-ray spectra. Including a new absorption component (such as a partially covering obscurer) does not significantly improve the fit to the data; $\Delta\text{C-stat}$ improvement of only 10 by fitting three more free parameters is not statistically reasonable for an additional component. We discuss the de-ionization of the warm-absorber in Section 4.2.

Interestingly, we find that the flux of the X-ray emission lines in NGC 3516 between the 2006 and 2017 observations has dropped significantly. The flux of the Fe K α line in the

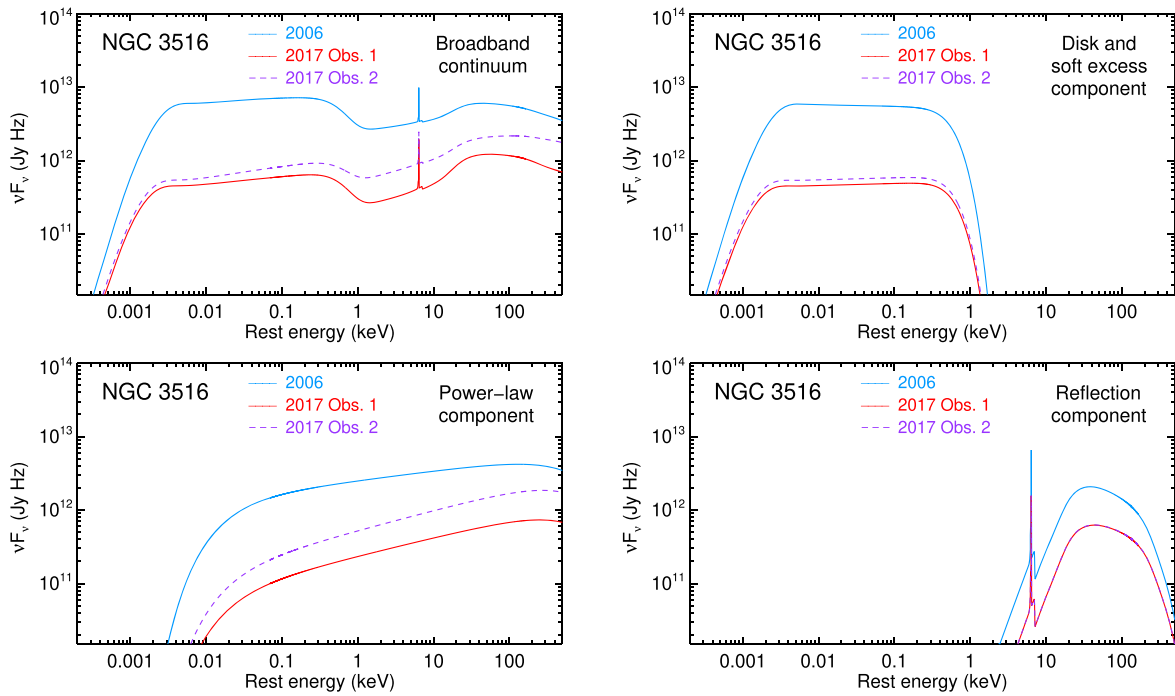


Figure 4. Derived intrinsic broadband SED model for the high-flux state (2006) and the low-flux state (2017) of NGC 3516. The total broadband continuum model is shown in the top left panel. The individual components of the SED model are displayed in the other panels: the disk and the soft X-ray excess component (`cont`, top right panel), the X-ray power-law continuum component (`pow`, bottom left panel), and the X-ray reflection component (`refl`, bottom right panel). All continuum components of the SED have become fainter in the new changing-look state of NGC 3516 in 2017.

Table 4
Best-fit Parameters of the Warm Absorber in NGC 3516

Parameter	2006	2017 Obs. 1	2017 Obs. 2
Comp 1:			
N_{H}	1.0 ± 0.2	1.0 (fixed)	1.0 (fixed)
$\log \xi$	2.8 ± 0.1	1.8 (de-ionized)	2.0 (de-ionized)
Comp 2:			
N_{H}	1.7 ± 0.2	1.7 (fixed)	1.7 (fixed)
$\log \xi$	2.2 ± 0.1	1.1 (de-ionized)	1.3 (de-ionized)
Comp 3:			
N_{H}	0.36 ± 0.01	0.36 (fixed)	0.36 (fixed)
$\log \xi$	0.8 ± 0.1	-0.5 (de-ionized)	-0.2 (de-ionized)

Note. Column density N_{H} is given in 10^{22} cm^{-2} . The model is based on the warm-absorber study of Mehdipour et al. (2010) using the 2006 XMM-Newton observation of NGC 3516 as described in Section 3.2. Because of the dimming of the ionizing continuum in 2017 (Figure 4), the warm-absorber becomes *de-ionized* as described in Section 3.2. This results in additional X-ray absorption by the warm-absorber as shown in Figure 5.

2006 XMM-Newton/EPIC-pn spectrum is $7.6 \pm 0.6 \times 10^{-13} \text{ erg cm}^{-2} \text{ s}^{-1}$ (this work; Mehdipour et al. 2010), while in the 2017 NuSTAR spectra, it is as follows: $1.9 \pm 0.2 \times 10^{-13} \text{ erg cm}^{-2} \text{ s}^{-1}$. In Mehdipour et al. (2010), we reported a narrow O VII forbidden emission line at 22.1 Å in the 2006 XMM-Newton/RGS spectrum, as well as another emission feature likely corresponding to a broad and blueshifted O VIII Ly α line. The new Chandra/LETG spectra suggest that these emission lines have also become intrinsically fainter in 2017. The LETG spectra only allow us to constrain an upper limit on the flux of each line ($< 2 \times 10^{-14} \text{ erg cm}^{-2} \text{ s}^{-1}$ for O VII, and $< 3 \times 10^{-14} \text{ erg cm}^{-2} \text{ s}^{-1}$ for O VIII), which is lower than the flux previously measured by Mehdipour et al. (2010) in the 2006

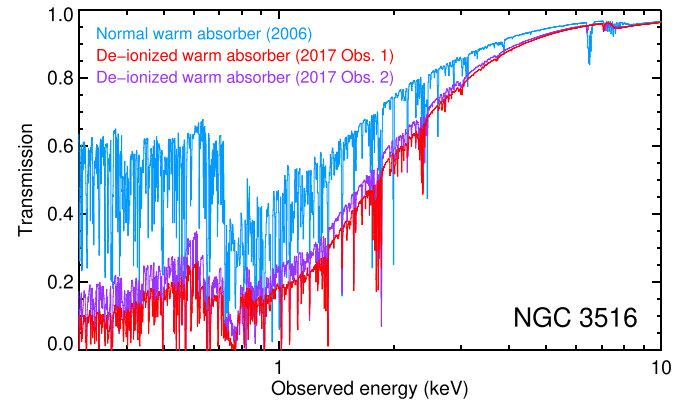


Figure 5. X-ray transmission (line and continuum absorption) of the NGC 3516 warm-absorber model in the high-flux state (2006) and the low-flux state (2017). The dimming of the ionizing SED (Figure 4) in 2017 causes *de-ionization* of the warm-absorber, thus resulting in stronger X-ray continuum absorption (shown above) and hence a harder X-ray spectrum (Figure 2). The transmission variability between Obs. 1 and 2, taken three weeks apart in 2017, is caused by variation in the ionization parameter ξ of the warm-absorber components in response to the intrinsic continuum variability. This warm-absorber transmission variability results in additional X-ray hardness variability (Figure 1).

high-flux state: $5 \pm 1 \times 10^{-14} \text{ erg cm}^{-2} \text{ s}^{-1}$ for O VII, and $8 \pm 1 \times 10^{-14} \text{ erg cm}^{-2} \text{ s}^{-1}$ for O VIII.

4. Discussion

4.1. Changing Look of the Broadband SED in NGC 3516

Ionized gas in AGN is widely accepted to be photoionized by the SED of the central ionizing source. Therefore, if this photoionizing SED changes, it is prudent to first consider the unavoidable effect of this change on the already-present ionized gas in an AGN, before assuming new additional gas

has appeared. The broadband (optical-UV-X-ray) continuum modeling presented in this paper shows that the ionizing SED in NGC 3516 has changed significantly (Figures 3 and 4). The natural consequence of this SED change on the ionized warm-absorber gas is an enhanced X-ray absorption by the warm-absorber according to photoionization computations (Figure 5). The corresponding absorption model (i.e., predicted from photoionization modeling) matches well the spectrum of NGC 3516 (Figure 3), without needing to include any new absorbing gas in the fit.

From only considering the goodness-of-fit in the X-ray band, it is not practical to conclusively discern between the changing-continuum and the obscuration models. The obscuring gas in principle can have multiple partially covering components with different ionization parameters and column densities (like found in NGC 5548 by Kaastra et al. 2014); thus by fitting these additional free parameters, similarly good fits can be achieved. The changing-continuum model, on the other hand, does not need additional free parameters to make a good fit, but rather the absorption is self-consistently predicted according to realistic photoionization modeling. Furthermore, because in NGC 3516 the flux level in the soft X-ray band is too low for high-resolution X-ray spectroscopy of absorption lines, one cannot analyze changes in the absorption lines, which is needed for a proper X-ray differentiation between the two models.

The X-ray obscuration scenario is limited in scope to the X-ray band and cannot explain the observed dimming of the optical/UV band at energies below the Lyman limit (Figures 3, left panels). Nor does it explain the dimming of the hard X-ray continuum at >3 keV as seen in our NuSTAR spectra (Figure 3, right panels). On the other hand, the changing-continuum model provides a plausible multi-wavelength solution that can explain all the observed data from optical/UV to X-rays. Importantly, NGC 3516 displays key differences from the established obscuration-event AGN, such as NGC 5548 (Kaastra et al. 2014) and NGC 3783 (Mehdipour et al. 2017), which also favor the changing-continuum explanation in NGC 3516 as described in the following.

Dramatic spectral changes, revealed by changing-look AGN, provide us with useful probes for studying the nature of accretion-powered radiation and outflows in AGN. An important characteristic of the changing-look event in NGC 3516 is the dimming of the intrinsic optical/UV continuum. This is in stark contrast to the transient-obscuration events found in the Seyfert-1 galaxies Mrk 335 (Longinotti et al. 2013), NGC 5548 (Kaastra et al. 2014), NGC 985 (Ebrero et al. 2016a), NGC 3783 (Mehdipour et al. 2017), Mrk 817 (Kara et al. 2021), and NGC 3227 (Mehdipour et al. 2021), where the optical/UV continuum does not become dimmer during the obscuration events. This supports our modeling of the optical/UV dimming in NGC 3516 as a change in the intrinsic continuum.

The diminished brightness of the X-ray spectrum is a common characteristic of both NGC 3516 and the obscured AGN, showing transformation into the spectrum of a typical Seyfert-2 galaxy, such as NGC 1068 (e.g., Grafton-Waters et al. 2021). However, in the obscuration-event AGN, their obscured and unobscured X-ray spectra are seen to converge toward hard X-rays, seen even in the case of strong obscuration in NGC 5548 (Kaastra et al. 2014). So the main difference between obscured and unobscured X-ray spectra is in the soft X-ray band where continuum absorption takes place, while the hard X-ray band is relatively unchanged. However, in NGC 3516, the whole of the

X-ray spectrum from soft to hard X-rays is significantly fainter than the historical observations. This suggests that the underlying broadband continuum in NGC 3516 has become intrinsically dimmer. Our modeling shows that all continuum components of the NGC 3516 SED have become fainter as a result of the changing-look phenomenon. This is a key difference to the obscuration-event AGN, where the underlying intrinsic SED does not show any major changes during the event (see, e.g., Mehdipour et al. 2015, 2017).

The behavior of AGN emission lines is another interesting distinction between NGC 3516 and the obscuration-event AGN. In NGC 3516, we find that the intrinsic luminosities of the Fe K α line, the O VII forbidden line, and the broad O VIII Ly α line, which were previously seen in the XMM-Newton EPIC-pn and RGS spectra (Mehdipour et al. 2010), have significantly dropped in 2017 as described in Section 3.2. This observed dimming of the X-ray emission lines is consistent with the changing-look behavior of the optical BLR emission lines in NGC 3516 (Shapovalova et al. 2019; Feng et al. 2021; Oknyansky et al. 2021), such as the clear order-of-magnitude drop in the flux of the H β line (Shapovalova et al. 2019). This is in stark contrast to the behavior of the obscuration-event AGN, where the emission lines remain unchanged. In the transient-obscuration-event AGN, where obscuration is likely only confined to our line of sight, the ionizing radiation that illuminates the BLR and the narrow-line region is not attenuated, and therefore, the strength of the optical and X-ray emission lines is not changed. This can be seen in the case of the transient-obscuration event in NGC 3783, where the X-ray emission lines stand prominently above the absorbed X-ray continuum in the XMM-Newton/RGS spectrum (Mao et al. 2019). In the extreme case of NGC 5548, where long-lasting and heavy obscuration has been persistently present for about a decade, some impacts on the AGN emission lines have been predicted if there is global obscuration in all directions (Dehghanian et al. 2019, 2021). However, the observed optical and X-ray emission lines in NGC 5548 have not noticeably changed (Kaastra et al. 2014; Mehdipour et al. 2015), certainly not to the extent of NGC 3516, and also the predicted line changes in NGC 5548 are less than the major line changes seen in NGC 3516. Therefore, in the case of NGC 3516, it is most likely that the intrinsic dimming of the ionizing continuum results in lower ionization and less reprocessing by the line-emitting regions.

As shown in Table 2, there is a significant drop in the normalization and the seed photon temperature T_{seed} of the Comptonized disk component (comt) in 2017 compared to 2006. The electron temperature T_e of the corona remains unchanged between the two epochs. The change in the comt component can be seen in Figure 4 (top right panel), where the luminosity of the thermal optical/UV emission from the disk is significantly lower during the 2017 observations. The dimming of the comt component also results in a much weaker soft X-ray excess component. The intrinsic luminosity of the soft X-ray excess over 0.3–1.5 keV was 6.7×10^{42} erg s $^{-1}$ in 2006, while it is significantly lower by a factor of 9 (Obs. 1) and 8 (Obs. 2) in 2017. Such major changes in the strength of the soft X-ray excess have previously been shown to be a key characteristic of changing-look AGN, such as Mrk 1018 (Noda & Done 2018). The soft X-ray excess, and its associated EUV emission, significantly contributes to the ionizing photons, and therefore, their vanishing or reemergence is shown to have a major impact on the appearance of the BLR lines in changing-

look AGN (Noda & Done 2018). Interestingly, the Swift monitoring (Figure 1) shows that in 2020, when NGC 3516 recovers to the high-flux state, as the UV flux peaks (top panel), the X-ray hardness ratio dips (bottom panel). Such X-ray spectral softening with UV brightening is a signature of the soft X-ray excess being produced by warm Comptonization, where the UV disk component and its emission tail at higher energies (i.e., the soft X-ray excess) become brighter together. This variability relation between the UV continuum and the soft X-ray excess has also been seen in other AGN, most notably Mrk 509 (Mehdipour et al. 2011).

The intrinsic X-ray power-law luminosity of NGC 3516 over 0.3–10 keV (1.7×10^{43} erg s⁻¹ in 2006) dropped by a factor of 10 (Obs. 1) and 4 (Obs. 2) in 2017. Also, the modeling results (Table 2) suggest that the intrinsic power-law continuum is slightly harder in the 2017 changing-look state. Furthermore, there is a decline in the reflection luminosity between the two epochs as shown in Figure 4 (bottom right panel) and in Table 3. This can be a manifestation of the primary X-ray continuum becoming dimmer in 2017 (Figure 4 and Table 3), hence producing less reprocessed emission. This behavior of the Fe K α line responding to the fading of the continuum has been seen before in other changing-look AGN, such as Mrk 1018 (LaMassa et al. 2017).

According to our broadband continuum modeling, we find that the intrinsic bolometric luminosity of NGC 3516 in its normal high-flux state in 2006 was 1.2×10^{44} erg s⁻¹, which, as a result of change in the accretion activity, dropped in the low-flux state to 1.5×10^{43} erg s⁻¹ (Obs. 1) and 2.7×10^{43} erg s⁻¹ (Obs. 2). Taking into account the black hole mass of $2.5 \times 10^7 M_{\odot}$ (Bentz & Katz 2015), the intrinsic bolometric luminosity of NGC 3516 corresponds to about 4% of the Eddington luminosity in the normal high-flux state (2006), and in the changing-look low-flux state (2017) to 0.5% (Obs. 1) and 0.9% (Obs. 2) of the Eddington luminosity. The observed timescale of the change in the production of seed photons from the accretion disk of NGC 3516 is indicative of being driven by thermal fluctuations from the disk (see, e.g., Kelly et al. 2009), rather than structural changes in the disk.

4.2. Effect of Dimming Continuum on Ionized Gas

Swift monitoring of NGC 3516 shows significant X-ray hardness variability (Figure 1, bottom panel). This is seen on both of the long timescales (between the high-flux and low-flux epochs), and on the short timescales (over a few weeks). The characteristics of the variability in NGC 3516 are similar to those found in AGN with *transient-obscuration events*, such as NGC 5548 (Mehdipour et al. 2016b), where obscuring outflows passing in our line of sight cause X-ray hardness variability. However, in the case of NGC 3516, we find that the variability is driven by the intrinsic continuum as shown by our modeling in this paper. As a consequence of the continuum variability, the ionization parameters of the warm-absorber components vary too, resulting in variation in their absorption, which would then contribute to the observed X-ray hardness variability (Figure 1). This can be seen by the transmission model in Figure 5, which shows that the continuum absorption by the warm-absorber is stronger in 2017 than in 2006, and on weeks timescales, it is stronger in Obs. 1 than in Obs. 2. These changes in the ionization of the warm-absorber, result in additional X-ray absorption and spectral hardness variability. Therefore, without taking into account the de-ionization of the

warm-absorber, one may erroneously fit a low-flux X-ray spectrum and its variability by introducing new additional obscuring gas, which we find not to be necessary in NGC 3516.

In Oknyansky et al. (2021), where the reverberation of the NGC 3516 optical emission lines is studied, based on the variable appearance of the Swift X-ray lightcurve, the authors suggest that there is a variable X-ray obscuration in NGC 3516. However, such a conclusion requires broadband spectral modeling and photoionization modeling, using X-ray spectra taken with Chandra or XMM-Newton, as well as hard X-ray spectral coverage with NuSTAR, which were not carried out in Oknyansky et al. (2021). Therefore, the effect of the changing ionizing SED on the already-present warm-absorber in NGC 3516 was not considered in Oknyansky et al. (2021). Nonetheless, our paper and Oknyansky et al. (2021) are both in agreement that “additional absorption” is needed to explain the data of NGC 3516; the difference is that in our paper we show that this “additional absorption” is a consequence of the dimming of the SED and hence the enhanced absorption by the de-ionized warm-absorber (Figure 5), whereas in Oknyansky et al. (2021) this effect is not considered, and instead the “additional absorption” is attributed to variable obscuration in our line of sight.

Adopting the scenario where the observed change in the X-ray emission lines is caused by a change in the ionizing SED, implies that the light travel time between the central ionizing source and the X-ray reprocessing regions must be less than the spacing between the two epochs (i.e., 2006 October and 2017 December). Therefore, the X-ray emission line regions are located within a distance $r < 3.4$ pc from the central source. In the case of O VII and O VIII emission lines, using the definition of ionization parameter ξ , the corresponding limit on density n_{H} can be estimated as $n_{\text{H}} = L_{\text{ion}}/\xi r^2$, where the ionizing luminosity L_{ion} is obtained from the broadband continuum modeling; the ionization parameter ξ is given by the `pion` model at which ionic concentrations of O VII ($\log \xi = 0.9$) and O VIII ($\log \xi = 1.7$) peak; and r is already constrained as described above. Thus, $r < 3.4$ pc implies that $n_{\text{H}} > 7 \times 10^4$ cm⁻³ for O VII, and $n_{\text{H}} > 1 \times 10^4$ cm⁻³ for the O VIII emission line region.

Since we find the warm-absorber responds to changes in the ionizing SED, we can put limits on its density n_{H} and distance r from the ionizing source, using the recombination timescale t_{rec} and the ionization parameter ξ . The `pion` photoionization model provides t_{rec} for each ion according to the definition of Bottorff et al. (2000). The distance is calculated as $r = \sqrt{L_{\text{ion}}/\xi n_{\text{H}}}$, where the ionizing luminosity L_{ion} is known from the SED modeling; the ionization parameter ξ is already given by the `pion` model; and n_{H} is constrained by the density-dependent t_{rec} . According to our modeling of NGC 3516, the warm-absorber components respond to the ionizing SED between the 2006 and 2017 epochs (i.e., de-ionization as a consequence of changing-look SED), as well as between Obs. 1 and 2 (separated by three weeks) as the intrinsic continuum varies. Since t_{rec} has to be shorter than the spacing between these observations, this can be used to put limits on n_{H} and hence r . For each component, we calculated t_{rec} for the strongest Oxygen ion with the highest ionic concentration. From the warm-absorber de-ionization between the 2006 and 2017 epochs, we find the following: $n_{\text{H}} > 930$ cm⁻³ and $r < 3.4$ pc for Comp 1; $n_{\text{H}} > 280$ cm⁻³ and $r < 12$ pc for Comp 2; $n_{\text{H}} > 290$ cm⁻³ and $r < 64$ pc for Comp 3. Furthermore, the

warm-absorber change on shorter timescales between Obs. 1 and 2 can be used to place tighter limits: $n_{\text{H}} > 1 \times 10^6 \text{ cm}^{-3}$ and $r < 0.1 \text{ pc}$ for Comp 1; $n_{\text{H}} > 9 \times 10^4 \text{ cm}^{-3}$ and $r < 0.8 \text{ pc}$ for Comp 2; $n_{\text{H}} > 5 \times 10^4 \text{ cm}^{-3}$ and $r < 6 \text{ pc}$ for Comp 3. These constraints on the distance of the warm-absorber, and the X-ray emission lines (Section 4.1), are comparable to those found for the ionized regions in NGC 5548 (Arav et al. 2015; Ebrero et al. 2016b; Mao et al. 2018).

A drop in the ionizing radiation that illuminates the absorbing gas in AGN could result in the appearance of new absorption lines in the UV and X-ray spectra as a consequence of the change in the photoionization equilibrium. However, it is almost always not possible to detect such new features in X-ray high-resolution spectra due to the low signal-to-noise ratio of the diminished X-ray continuum. In contrast, in the UV band, with HST, such features are often detectable (e.g., Kriss et al. 2019b). In the case of NGC 3516, no HST grating observations were taken during the epoch of the low-flux state. The last HST/COS observation of NGC 3516 was taken in 2011 January. The Swift lightcurve of NGC 3516 (Figure 1) shows that, in 2012, the optical/UV and X-ray fluxes were already dropping. While there are no Swift observations available over 2007–2011, it is possible that at the time of the 2011 HST observation, NGC 3516 was at the early stage of the changing-look event. Interestingly, the warm-absorber study of the 2011 HST/COS spectrum by Dunn et al. (2018) finds the appearance of new absorption troughs that were not present in previous UV spectra, as well as changes in the previously seen absorption troughs.

Historically, the UV spectra of NGC 3516 have shown considerable variability in the characteristics of the associated absorbing gas. Several decades ago, observations with the International Ultraviolet Explorer when NGC 3516 was in a high-flux state not only showed variability but also showed strong, broad, blueshifted absorption in C IV (Voit et al. 1987). Observations with the Hopkins Ultraviolet Telescope in 1995 also caught NGC 3516 in a bright state, but the broad C IV absorption troughs had disappeared (Kriss et al. 1996a). Mathur et al. 1997 suggested that the disappearance of the broad C IV absorption and the simultaneous diminution of the previously strong soft X-ray absorption were due to the expansion of the outflowing gas as it decreased in density and its ionization parameter rose. The broad absorption reappeared in 2000 as NGC 3516 entered a low-flux state, showing up as the “Component 5” (Kraemer et al. 2002). These same troughs are present in the 2011 HST/COS spectrum (Dunn et al. 2018) in addition to a new highly blueshifted “Component 9”. Although Dunn et al. (2018) interpret these spectral changes as the evolution of the outflows through bulk motion across our line of sight, the similarity to previous episodes of variability associated with significant changes in the flux state suggests that these spectral changes are primarily a change in the ionization state of the absorbing gas in the outflow.

5. Conclusions

In this paper, we studied the SED and the intrinsic X-ray absorption in NGC 3516 at two epochs, corresponding to its normal high-flux state (2006) and its changing-look low-flux state (2017). We modeled data taken with Chandra, NuSTAR, XMM-Newton, and Swift. The comparison of the modeling results for the two epochs enables us to ascertain how the accretion-powered radiation and the ionized outflows differ







between the two states of NGC 3516. Compared to its normal high-flux state in 2006, we find the intrinsic bolometric luminosity has dropped from $1.2 \times 10^{44} \text{ erg s}^{-1}$ by a factor of 4 to 8 during the timespan of our 2017 observations. This dimming of the multi-wavelength continuum is explained as a decline in the optical/UV seed photons from the accretion disk, which consequently translates into lower Compton up-scattering to X-rays. As a consequence of the dimming of the primary continuum, the reprocessed X-ray emission lines (Fe K α , O VII forbidden, and O VIII Ly α) have also become fainter in 2017. This implies that the corresponding X-ray emission line regions are located at $r < 3.4 \text{ pc}$ from the central source. The transformation of the ionizing continuum from a high-flux state to a low-flux state has a major impact on the ionization state of the ionized warm-absorber outflows. The change in the luminosity and the shape of the SED significantly lowers the ionization parameters of the three components of the warm-absorber in NGC 3516. This consequently results in enhanced X-ray absorption in our line of sight. Thus, variation in the ionization of the warm-absorber components, caused by intrinsic continuum variability, has a significant contribution to the observed X-ray spectral variability of NGC 3516, which is seen by the Swift monitoring on both short (weeks) and long (years) timescales. The response of the warm-absorber components to the ionizing SED implies that they are located at $r < 0.1 \text{ pc}$ for the highest-ionization component, $r < 0.8 \text{ pc}$ for the mid-ionization component, and $r < 6 \text{ pc}$ for the lowest-ionization component.

This research has made use of data obtained from the Chandra Data Archive, and software provided by the Chandra X-ray Center (CXC). This research has made use of data obtained with the NuSTAR mission, a project led by the California Institute of Technology (Caltech), managed by the Jet Propulsion Laboratory (JPL) and funded by NASA. This work is based on observations obtained with XMM-Newton, an ESA science mission with instruments and contributions directly funded by ESA Member States and the USA (NASA). Support for this work was provided by the National Aeronautics and Space Administration through Chandra Award Number 18103X issued by the Chandra X-ray Center, which is operated by the Smithsonian Astrophysical Observatory for and on behalf of the National Aeronautics Space Administration under contract NAS8-03060. SRON is supported financially by NWO, the Netherlands Organization for Scientific Research. We thank the anonymous referee for providing constructive comments and suggestions that improved the paper.

Facilities: CXO (LETG), NuSTAR, Swift, XMM.

Software: SPEX (Kaastra et al. 1996, 2020), HEASoft (Nasa High Energy Astrophysics Science Archive Research Center, or HEASARC, 2014).

ORCID iDs

Missagh Mehdipour  <https://orcid.org/0000-0002-4992-4664>
 Gerard A. Kriss  <https://orcid.org/0000-0002-2180-8266>
 Laura W. Brenneman  <https://orcid.org/0000-0003-2663-1954>
 Elisa Costantini  <https://orcid.org/0000-0001-8470-749X>
 Jelle S. Kaastra  <https://orcid.org/0000-0001-5540-2822>
 Graziella Branduardi-Raymont  <https://orcid.org/0000-0002-6620-6357>
 Jacobo Ebrero  <https://orcid.org/0000-0001-5924-8818>
 Junjie Mao  <https://orcid.org/0000-0001-7557-9713>

References

- Arav, N., Chamberlain, C., Kriss, G. A., et al. 2015, *A&A*, 577, A37
- Bentz, M. C., Denney, K. D., Grier, C. J., et al. 2013, *ApJ*, 767, 149
- Bentz, M. C., & Katz, S. 2015, *PASP*, 127, 67
- Bottoff, M. C., Korista, K. T., & Shlosman, I. 2000, *ApJ*, 537, 134
- Brinkman, A. C., Gunning, C. J. T., Kaastra, J. S., et al. 2000, *ApJL*, 530, L111
- Burrows, D. N., Hill, J. E., Nousek, J. A., et al. 2005, *SSRv*, 120, 165
- Cardelli, J. A., Clayton, G. C., & Mathis, J. S. 1989, *ApJ*, 345, 245
- Cash, W. 1979, *ApJ*, 228, 939
- Cohen, R. D., Rudy, R. J., Puetter, R. C., Ake, T. B., & Foltz, C. B. 1986, *ApJ*, 311, 135
- Costantini, E., Nicastro, F., Fruscione, A., et al. 2000, *ApJ*, 544, 283
- Crummey, J., Fabian, A. C., Gallo, L., & Ross, R. R. 2006, *MNRAS*, 365, 1067
- de Plaa, J., Kaastra, J. S., Tamura, T., et al. 2004, *A&A*, 423, 49
- Dehghanian, M., Ferland, G. J., Peterson, B. M., et al. 2019, *ApJL*, 882, L30
- Dehghanian, M., Ferland, G. J., Peterson, B. M., et al. 2021, *ApJ*, 906, 14
- Denney, K. D., De Rosa, G., Croxall, K., et al. 2014, *ApJ*, 796, 134
- Done, C., Davis, S. W., Jin, C., Blaes, O., & Ward, M. 2012, *MNRAS*, 420, 1848
- Dunn, J. P., Parvaresh, R., Kraemer, S. B., & Crenshaw, D. M. 2018, *ApJ*, 854, 166
- Ebrero, J., Kaastra, J. S., Kriss, G. A., et al. 2016b, *A&A*, 587, A129
- Ebrero, J., Kriss, G. A., Kaastra, J. S., & Ely, J. C. 2016a, *A&A*, 586, A72
- Elitzur, M., Ho, L. C., & Trump, J. R. 2014, *MNRAS*, 438, 3340
- Evans, P. A., Beardmore, A. P., Page, K. L., et al. 2007, *A&A*, 469, 379
- Evans, P. A., Beardmore, A. P., Page, K. L., et al. 2009, *MNRAS*, 397, 1177
- Feng, H.-C., Hu, C., Li, S.-S., et al. 2021, *ApJ*, 909, 18
- Ferrarese, L., & Merritt, D. 2000, *ApJL*, 539, L9
- Fruscione, A., McDowell, J. C., Allen, G. E., et al. 2006, *Proc. SPIE*, 6270, 62701V
- Gehrels, N., Chincarini, G., Giommi, P., et al. 2004, *ApJ*, 611, 1005
- Grafton-Waters, S., Branduardi-Raymont, G., Mehdipour, M., et al. 2021, *A&A*, 649, A162
- Harrison, F. A., Craig, W. W., Christensen, F. E., et al. 2013, *ApJ*, 770, 103
- Holzer, T., & Behar, E. 2012, *ApJ*, 747, 71
- Huerta, E. M., Krongold, Y., Nicastro, F., et al. 2014, *ApJ*, 793, 61
- Ilić, D., Oknyansky, V., Popović, L. Č., et al. 2020, *A&A*, 638, A13
- Kaastra, J. S. 2017, *A&A*, 605, A51
- Kaastra, J. S., & Bleeker, J. A. M. 2016, *A&A*, 587, A151
- Kaastra, J. S., Kriss, G. A., Cappi, M., et al. 2014, *Sci*, 345, 64
- Kaastra, J. S., Mewe, R., & Nieuwenhuijzen, H. 1996, in *UV and X-ray Spectroscopy of Astrophysical and Laboratory*, ed. K. Yamashita & T. Watanabe (Tokyo: Universal Academy), 411
- Kaastra, J. S., Raassen, A. J. J., de Plaa, J., & Gu, L. 2020, *SPEX X-ray spectral fitting package*, 3.06.01, Zenodo, doi:10.5281/zenodo.4384188
- Kara, E., Mehdipour, M., Kriss, G. A., et al. 2021, *ApJ*, 922, 151
- Keel, W. C. 1996, *AJ*, 111, 696
- Kelly, B. C., Bechtold, J., & Siemiginowska, A. 2009, *ApJ*, 698, 895
- Kinney, A. L., Calzetti, D., Bohlin, R. C., et al. 1996, *ApJ*, 467, 38
- Komossa, S. 2015, *JHEAp*, 7, 148
- Kraemer, S. B., Crenshaw, D. M., George, I. M., et al. 2002, *ApJ*, 577, 98
- Kriss, G. A., De Rosa, G., Ely, J., et al. 2019b, *ApJ*, 881, 153
- Kriss, G. A., Espey, B. R., Krolik, J. H., et al. 1996a, *ApJ*, 467, 622
- Kriss, G. A., Krolik, J. H., Otani, C., et al. 1996b, *ApJ*, 467, 629
- Kriss, G. A., Mehdipour, M., Kaastra, J. S., et al. 2019a, *A&A*, 621, A12
- Krolik, J. H., McKee, C. F., & Tarter, C. B. 1981, *ApJ*, 249, 422
- Kubota, A., & Done, C. 2018, *MNRAS*, 480, 1247
- Laha, S., Reynolds, C. S., Reeves, J., et al. 2021, *NaAs*, 5, 13
- LaMassa, S. M., Cales, S., Moran, E. C., et al. 2015, *ApJ*, 800, 144
- LaMassa, S. M., Yaqoob, T., & Kilgard, R. 2017, *ApJ*, 840, 11
- Lodders, K., Palme, H., & Gail, H.-P. 2009, *LanB*, 4B, 712
- Longinotti, A. L., Krongold, Y., Kriss, G. A., et al. 2013, *ApJ*, 766, 104
- MacLeod, C. L., Ross, N. P., Lawrence, A., et al. 2016, *MNRAS*, 457, 389
- Magdziarz, P., & Zdziarski, A. A. 1995, *MNRAS*, 273, 837
- Mao, J., Kaastra, J. S., Mehdipour, M., et al. 2018, *A&A*, 612, A18
- Mao, J., Mehdipour, M., Kaastra, J. S., et al. 2019, *A&A*, 621, A99
- Markowitz, A., Reeves, J. N., Miniutti, G., et al. 2008, *PASJ*, 60, 277
- Mathur, S., Wilkes, B. J., & Aldcroft, T. 1997, *ApJ*, 478, 182
- Matt, G., Guainazzi, M., & Maiolino, R. 2003, *MNRAS*, 342, 422
- Mehdipour, M., Branduardi-Raymont, G., Kaastra, J. S., et al. 2011, *A&A*, 534, A39
- Mehdipour, M., Branduardi-Raymont, G., & Page, M. J. 2010, *A&A*, 514, A100
- Mehdipour, M., Kaastra, J. S., & Kallman, T. 2016a, *A&A*, 596, A65
- Mehdipour, M., Kaastra, J. S., Kriss, G. A., et al. 2015, *A&A*, 575, A22
- Mehdipour, M., Kaastra, J. S., Kriss, G. A., et al. 2016b, *A&A*, 588, A139
- Mehdipour, M., Kaastra, J. S., Kriss, G. A., et al. 2017, *A&A*, 607, A28
- Mehdipour, M., Kriss, G. A., Kaastra, J. S., et al. 2021, *A&A*, 652, A150
- Merloni, A., Dwelly, T., Salvato, M., et al. 2015, *MNRAS*, 452, 69
- Miller, J. M., Kaastra, J. S., Miller, M. C., et al. 2015, *Natur*, 526, 542
- Nasa High Energy Astrophysics Science Archive Research Center (Heasarc) 2014, *HEASoft: Unified Release of FTOOLS and XANADU*, ascl:1408.004
- Netzer, H., Chelouche, D., George, I. M., et al. 2002, *ApJ*, 571, 256
- Noda, H., & Done, C. 2018, *MNRAS*, 480, 3898
- Noda, H., Minezaki, T., Watanabe, M., et al. 2016, *ApJ*, 828, 78
- O'Donnell, J. E. 1994, *ApJ*, 422, 158
- Oknyansky, V. L., Brotherton, M. S., Tsygankov, S. S., et al. 2021, *MNRAS*, 505, 1029
- Oknyansky, V. L., Winkler, H., Tsygankov, S. S., et al. 2019, *MNRAS*, 483, 558
- Petrucci, P. O., Gronkiewicz, D., Rozanska, A., et al. 2020, *A&A*, 634, A85
- Petrucci, P. O., Ursini, F., De Rosa, A., et al. 2018, *A&A*, 611, A59
- Poole, T. S., Breeveld, A. A., Page, M. J., et al. 2008, *MNRAS*, 383, 627
- Porquet, D., Reeves, J. N., Matt, G., et al. 2018, *A&A*, 609, A42
- Roming, P. W. A., Kennedy, T. E., Mason, K. O., et al. 2005, *SSRv*, 120, 95
- Ruan, J. J., Anderson, S. F., Cales, S. L., et al. 2016, *ApJ*, 826, 188
- Runnoe, J. C., Cales, S., Ruan, J. J., et al. 2016, *MNRAS*, 455, 1691
- Schlafly, E. F., & Finkbeiner, D. P. 2011, *ApJ*, 737, 103
- Shapovalova, A. I., Popović, L. Č., et al. 2019, *MNRAS*, 485, 4790
- Shappee, B. J., Prieto, J. L., Grupe, D., et al. 2014, *ApJ*, 788, 48
- Steenbrugge, K. C., Kaastra, J. S., Crenshaw, D. M., et al. 2005, *A&A*, 434, 569
- Trakhtenbrot, B., Arcavi, I., MacLeod, C. L., et al. 2019, *ApJ*, 883, 94
- Tran, H. D., Osterbrock, D. E., & Martel, A. 1992, *AJ*, 104, 2072
- Turner, T. J., Miller, L., Kraemer, S. B., & Reeves, J. N. 2011, *ApJ*, 733, 48
- Turner, T. J., Reeves, J. N., Kraemer, S. B., & Miller, L. 2008, *A&A*, 483, 161
- Voit, G. M., Shull, J. M., & Begelman, M. C. 1987, *ApJ*, 316, 573
- Willingale, R., Starling, R. L. C., Beardmore, A. P., Tanvir, N. R., & O'Brien, P. T. 2013, *MNRAS*, 431, 394
- Yang, Q., Wu, X.-B., Fan, X., et al. 2018, *ApJ*, 862, 109
- Zycki, P. T., & Czerny, B. 1994, *MNRAS*, 266, 653
- Zycki, P. T., Done, C., & Smith, D. A. 1999, *MNRAS*, 305, 231